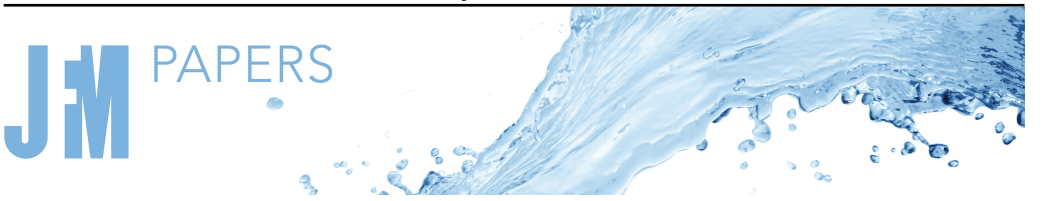
J. Fluid Mech. (2026), *vol.* 1031, A31, doi:10.1017/jfm.2026.11335



The dual-solution stability gap and dynamic transition from steady regular reflection to unstable Mach reflection

Xue-Ying Wang[1] **and Zi-Niu Wu**[1]

[1]Department of Engineering Mechanics, Tsinghua University, Beijing 100084, PR China

Corresponding author: Zi-Niu Wu, ziniuwu@mail.tsinghua.edu.cn

(Received 5 December 2025; revised 5 December 2025; accepted 18 February 2026)

For regular reflection (RR) and Mach reflection (MR), the critical parameter of the trailing-edge height ($H_{R,min}$), at which the reflected shock grazes the trailing edge, is the critical condition for stable and unstable reflection. A proof of the statement that $H_{R,min}$ for MR is larger than $H_{R,min}$ for RR, within some region in the dual-solution domain, is important for confirming the existence of a dual-solution stability gap, within which RR is stable while MR is unstable. This proof is accomplished here by transitivity, with the intermediate value corresponding to the minimum height of the Mach stem. By establishing a bridge between the evaluation of $H_{R,min}$ for MR and that of the linear coefficients for Mach stem height variation with the trailing-edge height, we overcome the difficulty of quantifying $H_{R,min}$ exactly, and show that the difference between $H_{R,min}$ for MR and $H_{R,min}$ for RR is significant, meaning that there is a large enough dual-solution stability gap. The confirmation of this gap has further impact on shock transition, suggesting a new transition scenario: stable to unstable dynamic transition, i.e., within the dual-solution stability gap, a stable RR can undergo a dynamic transition to an unstable MR state (unstart flow) under suitable disturbance of the flow parameters. This dynamic transition is demonstrated here numerically. The time history of dynamic transitions displays (i) direct transitions from RR to MR to unstart flow, with complex flow structures such as hybrid MR–type VI shock interference and double MR–MR reflections, and (ii) inverted transitions, in which RR first shifts to MR and then returns back to RR.

Key words: shock waves

© The Author(s), 2026. Published by Cambridge University Press. This is an Open Access article, distributed under the terms of the Creative Commons Attribution licence (https://creativecommons.org/licenses/by/4.0/), which permits unrestricted re-use, distribution and reproduction, provided the original article is properly cited.

https://doi.org/10.1017/jfm.2026.11335 Published online by Cambridge University Press

1. Introduction

The reflection of an incident shock over a reflecting surface is an important phenomenon in steady supersonic flow and has received a considerable amount of attention in studies since 1970s (see for instance Ben-Dor 2007). The critical condition at which regular reflection (RR) or Mach reflection (MR) occurs is one of the important issues that have been studied.

There are two classical transition criteria, the detachment condition and the von Neumann condition (von Neumann 1943). For a given inflow Mach number (denoted M_0 in this paper), if the wedge angle (denoted θ_w in this paper), i.e. the deflection angle of the wedge generating the incident shock wave, is larger than the detachment condition (denoted $\theta_w^{(D)}(M_0)$), then we necessarily have MR. If the wedge angle is smaller than the von Neumann condition (denoted $\theta_w^{(N)}(M_0)$), then we necessarily have RR. Note that inverted MR that corresponds to MR below the von Neumann condition (Henderson & Lozzi 1979; Hornung 1986; Hekiri & Emanuel 2015) may occur when there are additional influences such as downstream body (Roye *et al.* 1998), high downstream pressure (Ben-Dor *et al.* 1999), asymmetry shock reflection (Li *et al.* 1999) or a downstream incident shock (Guan *et al.* 2018), but this inverted MR will not be considered here.

There is a dual-solution domain in the plane (M_0, θ_w), since the detachment condition $(\theta_w = \theta_w^{(D)}(M_0))$ is above the von Neumann condition $(\theta_w = \theta_w^{(N)}(M_0))$. This means that when $\theta_w^{(N)}(M_0) < \theta_w < \theta_w^{(D)}(M_0)$, both RR and MR are possible. Although such a dual solution was recognised to be theoretically possible, great efforts have been required to clarify the real transition process.

Early studies only observed MR (cf. Henderson & Lozzi 1975; Hornung *et al.* 1979). The failure to observe RR led Hornung & Robinson (1982) to the conjecture that RR is unstable in the dual-solution domain. However, the stability analyses conducted by Teshukov (1989) and Li & Ben-Dor (1996) proved that RR should be stable. In fact, Hornung *et al.* (1979) hypothesised a hysteresis process, which means that, in the dual-solution domain, whether we have MR or RR depends on the history of the building of the actual steady flow. Then RR was observed numerically (Vuillon *et al.* 1995) and experimentally (Chpoun *et al.* 1995), where hysteresis occurs by changing the wedge angle. Later on a similar hysteresis was observed when the inflow Mach number changed from different directions (Ivanov *et al.*2001). More discussions about this hysteresis can be found in the papers of Ben-Dor *et al.* (2002) and Hornung (2014).

Apart from transition at the inflow Mach number or wedge angle crossing the boundaries of the dual-solution domain, dynamic transition within the dual-solution domain is also possible. For instance, RR may transit to MR if the amplitude of the disturbance exceeds a certain level, according to a number of studies (cf. Ivanov *et al.* 1997, 1998, 2000; Kudryavtsev *et al.* 2002; Li *et al.* 2011).

In the 1990s, it was discovered that stable MR is also subjected to geometric constraint. Vuillon *et al.* (1995) studied shock reflection for extremely low and large values of the trailing-edge height H_R (the distance of the wedge trailing edge (R) from the reflecting surface). Based on theoretical considerations, they found that the distance H_R is bounded by a lower limit $H_{R,min}$ and an upper limit $H_{R,max}$. According to Vuillon *et al.* (1995), the lower limit corresponds to the case in which the reflected shock wave (r) grazes the trailing edge (R). The upper limit is determined by the point where the leading characteristic of the trailing-edge expansion fan (denoted TEF) intersects the incident shock wave at the reflection point (G) for RR and at the triple point (T) for MR.

Consider first the upper limit. Vuillon *et al.* (1995) supposed that MR may transit to RR (Vuillon *et al.* 1995) for $H_R < H_{R,max}$, while Li & Ben-Dor (1997) found that

https://doi.org/10.1017/jfm.2026.11335 Published online by Cambridge University Press

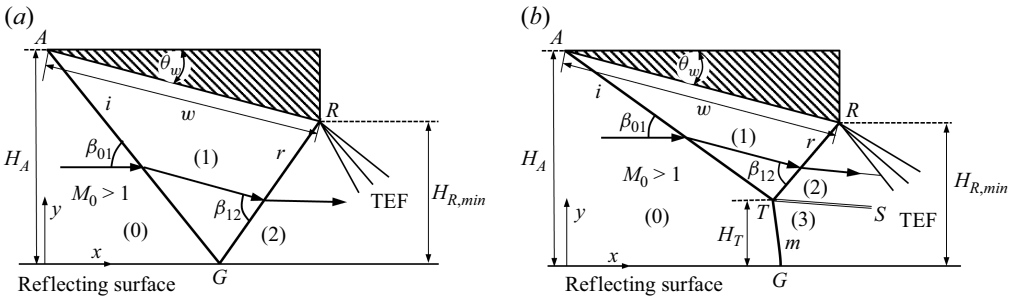


Figure 1. Shock reflection for $H_R = H_{R,min}$ at which the reflecting shock intersects the trailing edge R. Panels show (*a*) RR, (*b*) MR.

this transition occurs for $H_R > H_{R,max}$. Grasso & Paoli (1999) studied the effect of the geometrical set-up when accounting for shock reflection in non-equilibrium flow. Bai (2023) then provided the condition of H_R at which MR transits to RR, and found that, beyond $H_R = H_{R,max}$, the Mach stem height decreases nonlinearly with the trailing-edge height, until it vanishes at this new critical condition. Baby *et al.* (2024) studied the role of the interference between the trailing-edge expansion fan and the incident shock (occurring for a short wedge, or $H_R > H_{R,max}$) in the transition criteria between RR and MR. He & Shi (2025) studied the steady MR structure and the time evolution of transition from RR to MR under velocity perturbation, for $H_R > H_{R,max}$.

Now consider the shock reflection configuration at $H_R = H_{R,min}$ and this reflection configuration is schematically displayed in figure 1(*a*) for RR and figure 1(*b*) for MR. Vuillon *et al.* (1995) pointed out that, whenever the distance H_R reaches or is reduced below $H_{R,min}$, the MR becomes unstable and its Mach stem moves upstream until the MR vanishes and a bow shock wave is established ahead of the leading edge of the reflecting wedge. As a result, the flow through the two-dimensional converging nozzle, formed by the surface of the reflecting wedge and the line of symmetry, becomes subsonic. The two-dimensional converging nozzle which is formed by the wedge and bottom surfaces is said to be unstarted or choked. This process was indeed observed not only by their numerical simulations but also in experiments (Chpoun *et al.* 1995).

Li & Ben-Dor (1997) stated that $H_{R,min}^{(RR)}$ (lower limit for RR) is smaller than $H_{R,min}^{(MR)}$ (lower limit for MR). If $H_{R,min}^{(RR)} < H_{R,min}^{(MR)}$, then $H_{R,min}^{(RR)} < H_R < H_{R,min}^{(MR)}$ defines a dual-solution stability range, which means that, when $H_{R,min}^{(RR)} < H_R < H_{R,min}^{(MR)}$, RR is stable and MR is unstable. We call $H_{R,min}^{(RR)}$ and $H_{R,min}^{(MR)}$ the subcritical threshold and supercritical threshold for the geometric set-up, and call $\Delta H_{R,min} = H_{R,min}^{(MR)} - H_{R,min}^{(RR)}$ the dual-solution stability gap, which measures the width of the dual-solution stability range.

There are three issues which deserve further study. First, there lacks a formal proof for the inequality $H_{R,min}^{(MR)} > H_{R,min}^{(RR)}$ within the dual-solution domain. The existence of the Mach stem elevates the starting point of the reflected shock, but the reflected shock for MR has a smaller shock angle than that for RR; it is yet unknown whether these two counter-acting factors yield $H_{R,min}^{(MR)} > H_{R,min}^{(RR)}$ or $H_{R,min}^{(MR)} < H_{R,min}^{(RR)}$. A formal proof is useful to clarify this question. Second, there lacks a quantitatively correct method to estimate the gap $\Delta H_{R,min} = H_{R,min}^{(MR)} - H_{R,min}^{(RR)}$. Third, the inequality $H_{R,min}^{(MR)} > H_{R,min}^{(RR)}$ implies a new transition scenario, called the stable to unstable dynamic transition, not

https://doi.org/10.1017/jfm.2026.11335 Published online by Cambridge University Press

studied before: for H_R satisfying $H_{R,min}^{(RR)} < H_R < H_{R,min}^{(MR)}$, RR is stable while MR is unstable (in the sense that the flow will be unstarted or chocked, as pointed out by Vuillon *et al.* 1995).

This study addresses these three issues within the context of a two-dimensional inviscid flow.

The proof of $H_{R,min}^{(MR)} > H_{R,min}^{(RR)}$ is difficult since $H_{R,min}^{(MR)}$ involves the unknown Mach stem height H_T (see figure 1*b*). In § 2, we use the method of transitivity to prove the inequality $H_{R,min}^{(MR)} > H_{R,min}^{(RR)}$ formally, for part of the dual-solution domain. The intermediate value in transitivity proof is a lower bound related to the minimum possible Mach stem height.

There is also a difficulty in finding the quantitatively correct values of $H_{R,min}^{(MR)}$ and $\Delta H_{R,min}$, since the height $H_{R,min}^{(MR)}$ involves the unknown Mach stem height (H_T). In § 3, we propose a roadmap to find $H_{R,min}^{(MR)}$ and $\Delta H_{R,min}$. In the case that the Mach stem height varies linearly with respect to H_R, we derive an explicit formula for the dual-solution gap, by which $H_{R,min}^{(MR)}$ and $\Delta H_{R,min}$ can be determined correctly once the coefficients of the linear formula for Mach stem height are provided through, for instance, high fidelity numerical simulation.

In § 4, we study the third issue, steady to unsteady dynamic transition, using numerical simulation. We will demonstrate that, with the dual-solution stability gap, if the stable RR is subjected to large-amplitude disturbance, then this stable RR may transit dynamically to unstable MR, a phenomenon that appears to have not been mentioned before. Specifically, with a particular condition lying inside the dual-solution stability gap, we perform numerical simulation of the dynamic transition, to demonstrate this new type of dynamic transition. The results of this numerical study, including how to set up the perturbation and how the shock structure evolves in time to have the transition, will be given. This not only confirms the existence of the dual-solution stability gap, but also shows how the transition evolves dynamically and depends on the upstream disturbance.

Some results will be presented in terms of the relative trailing-edge height g defined by

$$g = \frac{H_R}{H_A}. \tag{1.1}$$

In terms of g, the lower limit is defined by

$$g_{min} = \frac{H_{R,min}}{H_A} \tag{1.2}$$

and the dual-solution stability gap is defined by

$$\Delta g_{min} = g_{min}^{(MR)} - g_{min}^{(RR)}, \tag{1.3}$$

where $g_{min}^{(RR)}$ is g_{min} for RR, and $g_{min}^{(MR)}$ is g_{min} for MR. The parameter g is linked to the length of the wedge lower surface (figure 1*a*) by the following obvious geometric relation:

$$w = \frac{H_A - H_R}{\sin\theta_w} = \frac{1-g}{\sin\theta_w} H_A \tag{1.4}$$

At $H_R = H_{R,min}$, expression (1.4) gives $w = w_{min}$, with

$$w_{min} = \frac{H_A - H_{R,min}}{\sin\theta_w} = \frac{1-g_{min}}{\sin\theta_w} H_A. \tag{1.5}$$

https://doi.org/10.1017/jfm.2026.11335 Published online by Cambridge University Press

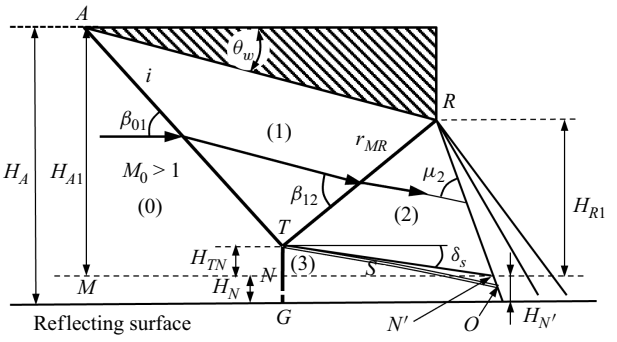


Figure 2. Schematic display for MR with various notations needed in the proof. The minimum Mach stem height(H_{NT}) is the Mach stem height at $H_N = 0$.

2. Proof of the inequality $g_{min}^{(MR)} > g_{min}^{(RR)}$ by transitivity

To prove the inequality $g_{min}^{(MR)} > g_{min}^{(RR)}$ or $H_{R,min}^{(MR)} > H_{R,min}^{(RR)}$, we use the method of transitivity. For this purpose, we need an intermediate value $g_{min}^{(int)}$ between $g_{min}^{(MR)}$ and $g_{min}^{(RR)}$, satisfying $g_{min}^{(MR)} > g_{min}^{(int)} > g_{min}^{(RR)}$. Here, we derive a lower bound $g_{min} = g_{min}^{(LB)}$ and use this lower bound as the intermediate value. This lower bound corresponds to the minimum Mach stem height.

2.1. *A lower bound for $g_{min}^{(MR)}$ corresponding to the minimum Mach stem height*

Now, we derive a lower bound which can be used as an intermediate value to prove the inequality $g_{min}^{(MR)} > g_{min}^{(RR)}$ or $H_{R,min}^{(MR)} > H_{R,min}^{(RR)}$ through transitivity.

Consider MR at $H_R = H_{R,min}$, as shown in figure 2. The slipline from the triple point T intersects the leading characteristic line of the trailing-edge expansion fan at point O. The tangent of the slipline at the triple point intersects the leading characteristic line of the trailing-edge expansion fan at point N'.

Let the height of N' with respect to the reflecting surface be $H_{N'}$. The Mach stem height H_T can be considered as composed of two segments

$$H_T = H_{TN} + H_N, \tag{2.1}$$

where $H_N = H_{N'}$, so

$$H_T = H_{TN} + H_{N'}. \tag{2.2}$$

Using the geometric relations displayed in figure 2, it can be shown that the condition such that the reflected shock grazes the trailing edge leads to

$$\frac{H_{A1} - H_{TN}}{\tan\beta_{01}} + \frac{H_{R1} - H_{TN}}{\tan(\beta_{12}^{MR} - \theta_w)} = \frac{H_{A1} - H_{R1}}{\tan\theta_w}. \tag{2.3}$$

The total length of the horizontal line *MN*', where *M* is the intersection of the line *NN*' and the vertical line passing the vertex *A*, is equal to the wedge horizontal length plus the horizontal projection of the leading characteristic line *RN*', so

$$\frac{H_{A1} - H_{TN}}{\tan\beta_{01}} + \frac{H_{TN}}{\tan\delta_s} = \frac{H_{A1} - H_{R1}}{\tan\theta_w} + \frac{H_{R1}}{\tan(\mu_2 + \delta_s)}, \tag{2.4}$$

where $\mu_2 = \arcsin(1/M_2)$ is the Mach angle of the leading characteristics of the trailing-edge expansion fan and δ_s is the slipline angle as marked in figure 2.

https://doi.org/10.1017/jfm.2026.11335 Published online by Cambridge University Press

Eliminating H_{TN} in (2.3) and (2.4) gives the following expression for H_{R1}/H_{A1}:

$$\frac{H_{R1}}{H_{A1}} = \frac{\dfrac{\psi t_2}{\sin\theta_w} + \dfrac{t_1}{\tan\theta_w} - \tan\delta_s}{t_2 + \dfrac{\psi t_2}{\sin\theta_w} + \dfrac{t_1}{\tan\theta_w} - \dfrac{t_1}{\tan(\mu_2+\delta_s)}}, \tag{2.5}$$

where $t_1 = \tan\beta_{01}\tan\delta_s$, $t_2 = \tan\beta_{01} - \tan\delta_s$ and ψ is defined by $\psi = (\sin(\beta_{12}^{MR} - \theta_w)\sin(\beta_{01} - \theta_w))/(\sin(\beta_{01} + \beta_{12}^{MR} - \theta_w))$. Here, β_{12}^{MR} is the shock angle of the reflected shock and β_{01} is the shock angle of the incident shock, and both shock angles can be determined by the triple point solution.

According to (1.2), we have

$$g_{min}^{MR} = \frac{H_{R1} + H_N}{H_{A1} + H_N}. \tag{2.6}$$

Since $H_N > 0$, we have

$$g_{min}^{MR} > g_{min}^{(LB)}, \tag{2.7}$$

where

$$g_{min}^{(LB)} = \frac{H_{R1}}{H_{A1}} \tag{2.8}$$

is the lower bound of g_{min}^{MR}. Here, H_{R1}/H_{A1} is given by (2.5).

2.2. *Proof of* $g_{min}^{(MR)} > g_{min}^{(LB)} > g_{min}^{(RR)}$

For RR (see figure 1*a*), Li & Ben-Dor (1997) give

$$H_{R,min}^{(RR)} = \phi^{RR} w, \tag{2.9}$$

with

$$\phi^{RR} = \frac{\sin(\beta_{12}^{RR} - \theta_w)\sin(\beta_{01} - \theta_w)}{\sin(\beta_{01} + \beta_{12}^{RR} - \theta_w)}. \tag{2.10}$$

Here, β_{12}^{RR} is the shock angle of the reflected shock.

At $H_R = H_{R,min}^{(RR)}$, we have $w = w_{min}$ where w_{min} is given by (1.5). Thus (2.9) should be replaced by

$$H_{R,min}^{(RR)} = \phi^{RR} w_{min}, \tag{2.11}$$

and, when (1.5) is used, we get

$$g_{min}^{(RR)} = \phi^{RR}\frac{1 - g_{min}^{(RR)}}{\sin\theta_w}, \tag{2.12}$$

which can be solved to give

$$g_{min}^{(RR)} = \frac{\phi^{RR}}{\sin\theta_w + \phi^{RR}}. \tag{2.13}$$

Once the lower bound $g_{min}^{(LB)}$ is obtained by (2.8), we can get the relative lower bound $\Delta g_{min}^{(LB)}$ through

$$\Delta g_{min}^{(LB)} = g_{min}^{(LB)} - g_{min}^{(RR)}. \tag{2.14}$$

https://doi.org/10.1017/jfm.2026.11335 Published online by Cambridge University Press

The algorithm to find the lower bound $g_{min}^{(LB)}$ involves flow parameters that are determined by shock wave relations. For this purpose, we first introduce the classical shock wave expressions.

We use u to denote the upstream flow condition of an oblique shock wave, and d to denote the downstream flow condition. The shock angle β_{ud} is related to the flow deflection angle θ_{ud} through the shock angle relation

$$\tan\theta_{ud} = f_\theta(M_u, \beta_{ud}), \tag{2.15}$$

where

$$f_\theta(M, \beta) = \frac{2\left(M^2\sin^2\beta - 1\right)}{\left(M^2\left(\gamma + \cos 2\beta\right) + 2\right)\tan\beta}. \tag{2.16}$$

For given $M_u > 1$ and θ_{ud} (below the detached angle), the relation (2.15) admits two solutions for β_{ud}; the smaller one is called the weak solution, and the larger one is the strong solution.

The Mach number M_u is then given by the shock relation for Mach number

$$M_d = f_M(M_u, \beta_{ud}), \tag{2.17}$$

where

$$f_M(M, \beta) = \sqrt{\frac{(\gamma-1)M^2 + 2}{2\gamma M^2\sin^2\beta - (\gamma-1)} + \frac{2M^2\cos^2\beta}{(\gamma-1)M^2\sin^2\beta + 2}}. \tag{2.18}$$

Also, the pressure is given by the shock relation for pressure

$$p_d = p_u f_p(M_u, \beta_{ud}), \tag{2.19}$$

where

$$f_p(M, \beta) = 1 + \frac{2\gamma}{\gamma+1}\left(M^2\sin^2\beta - 1\right). \tag{2.20}$$

Now we outline the algorithm to find the lower bound $g_{min}^{(LB)}$.

Step 1. Consider any point M_0 and θ_w inside the dual-solution domain. Use the oblique wave expression to find the solution in region (1) of figure 2. Find the shock angle β_{01} by solving $\tan\theta_w = f_\theta(M_0, \beta_{01})$ for the weak solution. Find M_1 and p_1 by solving $M_1 = f_M(M_0, \beta_{01})$ and $p_1 = p_0 f_p(M_0, \beta_{01})$

Step 2. Find g_{min}^{RR} through (2.13). For this purpose, we first solve for the two shock theory for RR to find β_{12}^{RR}. The shock angle β_{12}^{RR} is obtained by solving $\tan\theta_w = f_\theta(M_1, \beta_{12}^{RR})$ for the weak solution. The expression (2.10) for ϕ^{RR} that appears in (2.13) can then be computed, so we obtain $g_{min}^{(RR)}$ through (2.13).

Step 3. Find $g_{min}^{(LB)}$ through (2.8). To do this, we first need to find the triple point solution. Using the flow parallel conditions $\theta_{12} = \theta_w - \delta_s$, $\theta_{03} = \delta_s$ and the pressure balance relation $p_3^{MR} = p_2^{MR}$, we solve

$$\tan\theta_{12} = f_\theta(M_1, \beta_{12}^{MR}),\ p_2^{MR} = p_1 f_p(M_1, \beta_{12}^{MR}) \text{ (weak solution)}, \tag{2.21}$$

and

$$\tan\theta_{03} = f_\theta(M_0, \beta_{03}^{MR}),\ p_3^{MR} = p_0 f_p(M_0, \beta_{03}^{MR}) \text{ (strong solution)}. \tag{2.22}$$

Then, (2.5) is used for H_{R1}/H_{A1}. Finally, we get $g_{min}^{(LB)}$ through (2.8).

https://doi.org/10.1017/jfm.2026.11335 Published online by Cambridge University Press

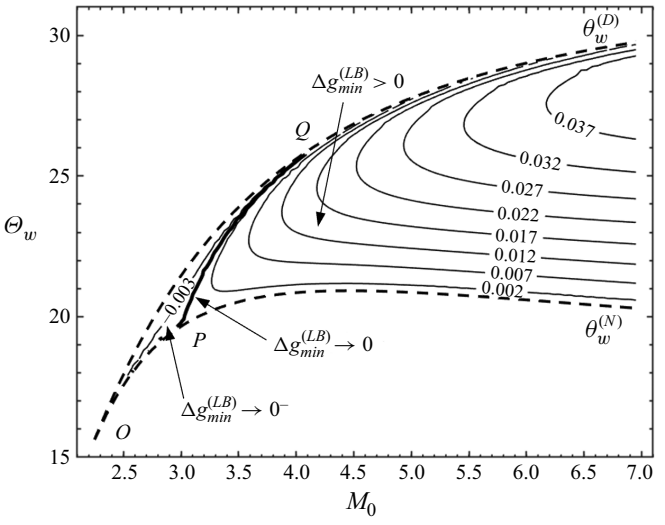


Figure 3 Contourlines of the relative lower bound $\Delta g_{min}^{(LB)}$ in the dual-solution domain. The tip horn region is defined as the region OPQ with $\Delta g_{min}^{(LB)} \to 0$.

Step 4. Finally, we get $\Delta g_{min}^{(LB)}$ through (2.14). For other M_0 and θ_w, go to step 1 and repeat step 2 to step 4.

The lower bound $\Delta g_{min}^{(LB)}$ thus obtained for M_0 and θ_w lying inside the dual-solution domain is shown in figure 3. We see that $\Delta g_{min}^{(LB)}$ is away from zero in the dual-solution domain except for the tip horn region (OPQ) which is near the left boundary of this dual-solution domain.

Thus we have shown that the inequality $\Delta g_{min}^{(LB)} > 0$ and thus

$$g_{min}^{(LB)} > g_{min}^{(RR)} \tag{2.23}$$

holds within the dual-solution domain except in the tip horn region. Note that tip horn region is small.

By transitivity through (2.7) and (2.23), the inequality

$$g_{min}^{(MR)} > g_{min}^{(RR)} \tag{2.24}$$

holds and thus $H_{R,min}^{(MR)} > H_{R,min}^{(RR)}$ holds, within the dual-solution domain, except inside the tip horn region.

3. A method to determine the quantitative values of $g_{min}^{(MR)}$ and Δg_{min}

The lower bound of the dual-solution stability gap derived in § 2 has been used as an intermediate value for proof by transitivity. The real value of this gap should be greater than this lower bound. Here, we provide a method to derive the quantitative value of this gap once M_0 and θ_w are given.

https://doi.org/10.1017/jfm.2026.11335 Published online by Cambridge University Press

3.1. *A road map to find $g_{min}^{(MR)}$ and Δg_{min}*

For MR with Mach stem height H_T (see figure 1*b*), Li & Ben-Dor (1997) give the following expression for $H_{R,min}^{(MR)}$:

$$H_{R,min}^{(MR)} = H_T + \phi^{MR} w, \tag{3.1}$$

where

$$\phi^{MR} = \frac{\sin(\beta_{12}^{MR} - \theta_w)\sin(\beta_{01} - \theta_w)}{\sin(\beta_{01} + \beta_{12}^{MR} - \theta_w)}. \tag{3.2}$$

Here, β_{12}^{MR} is the shock angle of the reflected shock in case of MR.

However, (3.1) cannot be directly applied here. The reason is that $H_T = H_{T,min}$ and $w = w_{min}$ (see (1.5) for w_{min}) at $H_R = H_{R,min}^{(MR)}$, so expression (3.1) should be replaced by

$$H_{R,min}^{(MR)} = H_{T,min} + \phi^{MR} w_{min}. \tag{3.3}$$

We define the relative Mach stem height as $h_T = H_T/H_A$. Using $H_{T,min} = h_{T,min} H_A$ and (1.5) in (3.3), and replacing $H_{R,min}^{(MR)}$ by $g_{min}^{(MR)} H_A$, we obtain the following expression for $g_{min}^{(MR)}$:

$$g_{min}^{(MR)} = h_{T,min} + \frac{\phi^{MR}}{\sin\theta_w}\left(1 - g_{min}^{(MR)}\right), \tag{3.4}$$

where ϕ^{MR} is given by (3.2).

According to Hornung & Robinson (1982), $H_T/w = h(M_0, \theta_w, (H_R/w))$, which can be equivalently written as

$$h_T = h_T\,(M_0, \theta_w, g) \tag{3.5}$$

due to (1.4). Note that the functional form also depends on γ, the ratio of the specific heats. Here, we do not consider varying γ so this parameter is considered as a constant in (3.5).

Putting $g = g_{min}^{(MR)}$ and $h_T = h_{T,min}$ in (3.5), we have

$$h_{T,min} = h_T\left(M_0, \theta_w, g_{min}^{(MR)}\right). \tag{3.6}$$

Since $h_{T,min}$ and $\phi^{MR}/\sin\theta_w$ are functions of M_0 and θ_w, expression (3.4) means that $g_{min}^{(MR)}$ is a function of M_0 and θ_w.

Then (3.4) can be solved for $g_{min}^{(MR)}$ if we know expression (3.6).

3.2. *Efficient method for $g_{min}^{(MR)}$ and Δg_{min} when h_T is a linear function of g*

Li & Ben-Dor (1997) stated that the calculations of Vuillon *et al.* (1995) indicated that, within the forth-order approximation, the trajectory of the Mach stem foot (similar to point G in figure 1*b*) is a straight line, meaning that the Mach stem height may decrease linearly with H_R. Schotz *et al.*(1997, equation (21)) and Bai & Wu (2021) also suggested equivalent linear variation.

Bai & Wu (2021) considered several conditions and showed, through high fidelity numerical simulation, that the relative Mach stem height can be fitted by a linear formula, i.e.

$$h_T = Ag + B \tag{3.7}$$

https://doi.org/10.1017/jfm.2026.11335 Published online by Cambridge University Press

Case	M_0, θ_w	A	B	origin	R^2	Grid
1	$4, 25^o$	-1.031	0.723	Bai & Wu (2021)	0.9994	400×600
2	$3, 21^o$	-0.514	0.403	Present	0.9998	400×800
3	$5, 25^o$	-0.908	0.560	Present	0.9999	400×800

Table 1. The coefficients A and B for three cases. Case 1 is from Bai & Wu (2021). Case 2 is from the present calculation with $g = 0.45, 0.50, 0.55, 0.60$. Case 3 is from the present calculation with $g = 0.45, 0.50, 0.55, 0.60$.

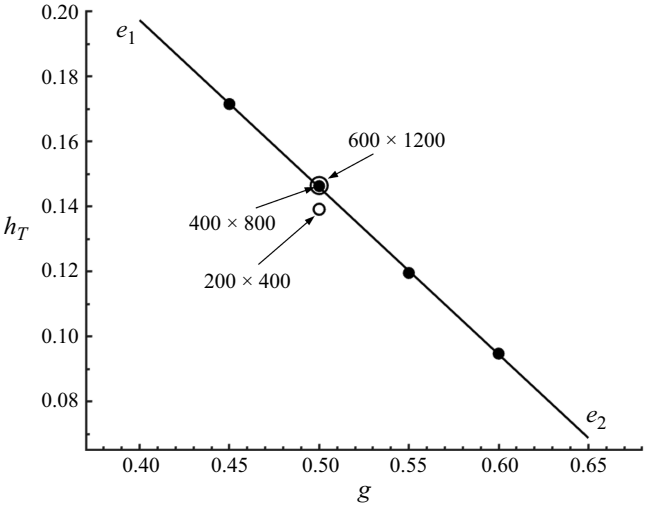


Figure 4. Numerical results of the normalised Mach stem heights as functions of g for case 2.The line e_1e_2 is a straight line passing through Computational Fluid Dynamics (CFD) data. Open circles are CFD data using different grids.

in terms of the present notations. The linear formula fits the numerical results with R^2 above 0.99, where R^2 stands for the linear correlation coefficient.

Only one condition considered by Bai & Wu (2021) lies within the dual-solution domain. Here, we added two more cases in the dual-solution domain, with A and B determined by numerical simulation using the Fluent package with the choice of second-order Roe scheme in the same way as Bai & Wu (2021) but we increase the number grid points in the horizontal direction since the geometry is longer in the present calculation. The condition by Bai & Wu (2021) and the two new cases are shown in table 1.

Note that Bai & Wu (2021) suggested the grid number after grid convergence study. Here, we follow the same approach and display in figure 4 the relative Mach stem heights obtained by numerical simulation with four different values of g. The numerical results are marked with black circles, the additional marks in figure 4 show that numerical results with a grid of 400×800 points are acceptable since further refining the grid does not change the Mach stem height noticeably.

Similarly to case 1 studied by Bai & Wu (2021), the normalised Mach stem height is almost linear with respect to g. In figure 4, a straight line e_1e_2 is marked across the numerical data and this straight line is given by (3.7), with A and B shown in table 1. For case 3, we also have similar behaviour and the fitted coefficients A and B are shown in table 1. In all cases, the linear form (3.7) holds with $R^2 > 0.99$.

https://doi.org/10.1017/jfm.2026.11335 Published online by Cambridge University Press

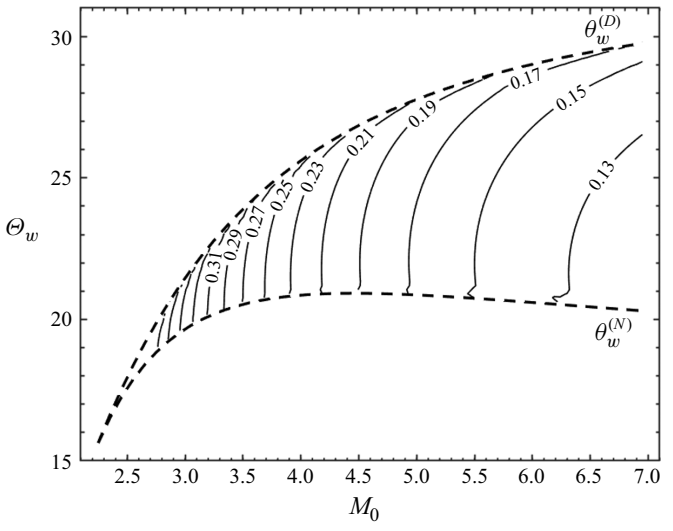


Figure 5. Contourlines of $g_{min}^{(RR)}$ in the dual-solution domain. This value is given by the exact formula (2.13).

In conditions such that the relative Mach stem height follows the linear form (3.7), we have

$$h_{T,min} = A g_{min}^{(MR)} + B \tag{3.8}$$

so that the expression (3.4) can be solved to give the following explicit expression for $g_{min}^{(MR)}$:

$$\overline{g}_{min}^{(MR)} = \frac{\dfrac{\phi^{MR}}{\sin\theta_w} + B}{1 - A + \dfrac{\phi^{MR}}{\sin\theta_w}}, \tag{3.9}$$

where $\overline{g}_{min}^{(MR)}$ denotes $g_{min}^{(MR)}$ when (3.8) is applied.

3.3. *Predicted values of $\overline{g}_{min}^{(MR)}$ and $\triangle\overline{g}_{min}$ for three cases*

For a given condition (M_0, θ_w), if (3.7) holds and if the exact values of A and B are known (e.g. from high fidelity numerical simulation), then (3.9) yields the required values of $g_{min}^{(MR)} = \overline{g}_{min}^{(MR)}$, and hence the required values of $\triangle g_{min} = \triangle\overline{g}_{min}$, where

$$\triangle\overline{g}_{min} = \overline{g}_{min}^{(MR)} - g_{min}^{(RR)}, \tag{3.10}$$

with $g_{min}^{(RR)}$ computed by (2.13). The quantity $g_{min}^{(RR)}$ computed by the exact expression (2.13) is shown in figure 5.

Table 2 gives $\overline{g}_{min}^{(MR)}$ and $\triangle\overline{g}_{min}$ thus obtained.

Now let us give some details for case 1. Using (2.13), we get, for $M_0 = 4$, $\theta_w = 25^o$,

$$g_{min}^{(RR)} = 0.239. \tag{3.11}$$

With $A = -1.031$ and $B = 0.723$ from table 1, we get from (3.9) the value

$$\overline{g}_{min}^{(MR)} = 0.417. \tag{3.12}$$

https://doi.org/10.1017/jfm.2026.11335 Published online by Cambridge University Press

Case	M_0, θ_w	ϕ^{RR}, ϕ^{MR} Expr. (2.10), (3.2)	$g_{min}^{(RR)}$ Expr. (2.13)	$\overline{g}_{min}^{(MR)}$ Expr. (3.9)	$\Delta\overline{g}_{min}$ Expr. (3.10)
1	$4, 25^o$	0.133, 0.091	0.239	0.417	0.178
2	$3, 21^o$	0.194, 0.171	0.351	0.442	0.091
3	$5, 25^o$	0.089, 0.061	0.173	0.358	0.185

Table 2. Predicted values of $\overline{g}_{min}^{(MR)}$ and $\Delta\overline{g}_{min}$ for the three cases shown in table 1.

Case	M_0, θ_w	$\overline{g}_{min}^{(MR)}$	$g_{min,CFD}^{l}$	$g_{min,CFD}^{u}$	$g_{min,CFD}$	100ϵ
1	$4, 25^o$	0.417	0.420	0.425	0.4225 ± 0.0025	1.32 ± 0.60
2	$3, 21^o$	0.442	0.440	0.450	0.445 ± 0.005	0.68 ± 1.13
3	$5, 25^o$	0.358	0.350	0.360	0.355 ± 0.005	0.84 ± 1.40

Table 3. The values of $g_{min,CFD}^{l}$, $g_{min,CFD}^{u}$, $g_{min,CFD}$ and ε for the three cases.

Hence, for case 1,

$$\Delta\overline{g}_{min} = 0.178. \tag{3.13}$$

3.4. *Numerical validation*

Now we perform numerical simulation, using the same numerical approach as stated above, to check the predicted quantities of $\overline{g}_{min}^{(MR)}$ and $\Delta\overline{g}_{min}$. To do this, we seek a $g = g_{min,CFD}^{l}$ value near $\overline{g}_{min}^{(MR)}$ for which we get a unstable MR numerical solution, and a $g = g_{min,CFD}^{u}$ value near $\overline{g}_{min}^{(MR)}$ for which we get a stable MR numerical solution. Once $g_{min,CFD}^{u}$ is close to $g_{min,CFD}^{l}$, we may say that $g_{min}^{(MR)}$ predicted by numerical simulation is

$$g_{min,CFD} = \frac{1}{2}(g_{min,CFD}^{u} + g_{min,CFD}^{l}). \tag{3.14}$$

The difference between the predicted value $\overline{g}_{min}^{(MR)}$ and $g_{min,CFD}$ is defined by

$$\varepsilon = \frac{g_{min,CFD} - \overline{g}_{min}^{(MR)}}{\overline{g}_{min}^{(MR)}}. \tag{3.15}$$

The values of $g_{min,CFD}^{l}$, $g_{min,CFD}^{u}$, $g_{min,CFD}$ and ε are shown in table 3. The Mach number contourlines at $g = g_{min,CFD}^{l}$ and $g = g_{min,CFD}^{u}$ are displayed in figures 6, 7 and 8 for cases 1, 2 and 3. Note that for $g = g_{min,CFD}^{l}$ the flow is unstable, so figures 6(*a*), 7(*a*) and 8(*a*) are a snapshot of the time-dependent result.

According to table 3, $\overline{g}_{min}^{(MR)}$ is very close to $g_{min,CFD}$, with a relative difference less than 2 %. Consider for instance case 1, where the predicted value for $g_{min}^{(MR)}$ is $\overline{g}_{min}^{(MR)} = 0.417$ (see (3.12)), while the numerical simulation gives $g_{min,CFD} = 0.4225 \pm 0.0025$. The difference is $\varepsilon = 1.32\,\% \pm 0.60\,\%$. Note that $g_{min,CFD}^{l}$ and $g_{min,CFD}^{u}$ are both (slightly) larger than $\overline{g}_{min}^{(MR)}$ (possibly due to numerical error). For case 2 and case 3, we have $g_{min,CFD}^{l} < \overline{g}_{min}^{(MR)} < g_{min,CFD}^{u}$.

https://doi.org/10.1017/jfm.2026.11335 Published online by Cambridge University Press

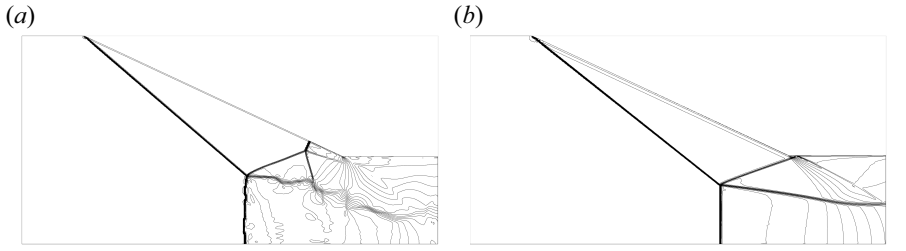


Figure 6. Mach number contours for case 1: (*a*) $g = 0.420$, (*b*) $g = 0.425$.

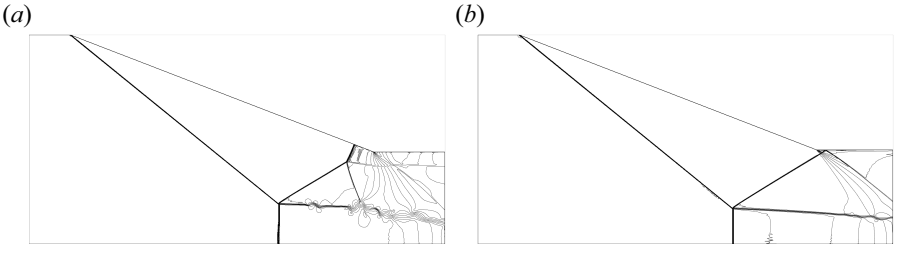


Figure 7. Mach number contours for case 2: (*a*) $g = 0.440$, (*b*) $g = 0.450$.

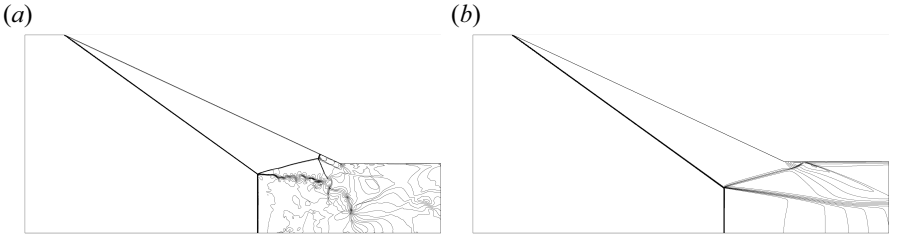


Figure 8. Mach number contours for case 3: (*a*) $g = 0.350$, (*b*) $g = 0.360$.

4. Dynamic transition from stable regular reflection to unstable Mach reflection within the dual-solution stability gap

The objective of this section is to demonstrate a new type of dynamic transition within the dual-solution stability gap, using numerical simulation, and to display possible shock reflection or interaction patterns during the process of dynamic transition.

4.1. *Dynamic transition problem*

We have shown in § 3 that, within a large part of the dual-solution domain, the supercritical geometric threshold $g_{min}^{(MR)}$ is larger than the subcritical one $g_{min}^{(RR)}$, i.e. there exists a dual-solution stability gap $\triangle g_{min} = g_{min}^{(MR)} - g_{min}^{(RR)} > 0$ within the dual-solution domain except for its tip horn region. This means that, at any point (M_0, θ_w) within this region, if the relative trailing-edge height g satisfies

$$g_{min}^{(RR)} < g < g_{min}^{(MR)}, \tag{4.1}$$

then the RR solution is stable, and the MR solution is unstable. This would mean a new dynamic transition possibility: stable RR may transit to unstable MR when there is large-amplitude disturbance.

https://doi.org/10.1017/jfm.2026.11335 Published online by Cambridge University Press

Before this is made clearer, we recall what happens in conventional dynamic transition, for which stable RR transits to stable MR by large-amplitude disturbance, for g outside the dual-solution stability gap.

It is known that, in the dual-solution domain, RR may transit to MR if the amplitude of the disturbance exceeds a certain level (Ivanov *et al.* 1997, 1998, 2000). The dynamic transition process can be understood by following the time history of this transition using numerical simulation. Various forms of disturbance have been considered. Ivanov *et al.* (1997) considered disturbances in the form of strong short-time changes in the free-stream velocity. Kudyavtev *et al.* (2002) used three types of upstream perturbation: inlet pressure wave disturbances (including shock waves and rarefaction waves), inlet contact discontinuity disturbances and localised density disturbances. All these types of disturbances have been shown to be able to cause dynamic transition from RR to MR.

The dynamic transition process has been also studied theoretically. Mouton & Hornung (2007) assumed a single but evolutionary MR, which satisfies a steady flow model when the reference frame is attached to the moving triple point, and built a dynamic transition model that tracks the growth of Mach stem height during the transition. Li *et al.* (2011) followed the work of Mouton & Hornung (2007) and included more fine structures than a single unsteady MR to build a dynamic transition model. They also used a local discontinuity to force the transition from RR to MR, and the initial-period Riemann solution of the local discontinuity interacted with the initial RR to evolve the flow to steady MR. He & Shi (2025) studied dynamic transition from RR to MR under velocity perturbation, for $H_R > H_{R,max}$. The evolution of the Mach stem height was predicted theoretically, when the effect of the trailing-edge expansion fan was considered.

The present study is concerned with dynamic transition from RR to MR due to local disturbance. Felthun & Skews (2002) and Felthun & Skews (2004) examined the transition dynamics between RR and MR, when the wedge angle is changing in time. Margha *et al.* (2023) investigated the dynamic transition of unsteady supersonic flow from MR to RR over a horizontally moving wedge. Naidoo & Skews (2011) studied dynamic transition from RR to MR when the wedge is rapidly rotating. Naidoo & Skews (2014) examined the effects of wedge rotation on dynamic transition from MR to RR. Goyal *et al.* (2021) also studied the dynamic effects in the transition from RR to MR when the wedge is rotating, notably, they considered the effect of wedge rotation speeds on the transition conditions, the growth rate of the Mach stem and motion of the reflection point.

4.2. *Dual-solution unstable condition and disturbance to inaugurate dynamic transition*

Here, we consider dynamic transition in the dual-solution domain, for a geometrical set-up which has a trailing-edge height above the lower limit $H_{R,min}$ for RR, but below the lower limit $H_{R,min}$ for MR. In this situation, RR should transit to unstable MR, unlike the dynamic transition previously studied, in which RR transits to stable MR.

For numerical simulation, we choose the specific condition $M_0 = 4$, $\theta_w = 25^o$. We have shown, in § 3.3, that

$$g_{min}^{(RR)} = 0.239,\ g_{min}^{(MR)} = 0.417, \tag{4.2}$$

for this condition. Thus, if we choose a g such that $0.239 < g < 0.417$, then under some disturbance, RR could transit to unstable MR, in contrast to the transition from RR to stable MR studied earlier for which g is above the lower limit. The value $g = 0.328$ meets such a condition, i.e. with $g = 0.328$, RR could transit to unstable MR.

Following Kudyavtev *et al.* (2002), we use a contact discontinuity disturbance at the inlet. Starting from the steady numerical solution of RR, we put in the inlet, for a time

https://doi.org/10.1017/jfm.2026.11335 Published online by Cambridge University Press

Case	Disturbance	$\Delta\rho/\rho_0$	M'	$\tau_{disturb}$	Transition mode
1	Localised	−0.250	3.464	0.069	Failed (with RR → perturbed RR → RR)
2	Localised	−0.375	3.162	0.069	Success (with RR → MR → unstart)
3	Localised	−0.500	2.828	0.069	Success (with RR → MR → unstart)
4	Localised	−0.250	3.464	0.121	Success (with RR → MR → unstart)
5	Localised	−0.250	3.464	0.174	Success (with RR → MR → unstart)
6	Localised	−0.438	3.000	0.296	Success (with RR → MR + type IV SI → unstart)
7	Full inlet	−0.438	3.000	0.174	Failed (with RR → MR → RR)

Table 4. Dynamic transition in the double solution domain with $(M_0, \theta_w) = (4, 25^o)$ (at which $g^{RR}_{min} = 0.239$, $g^{MR}_{min} = 0.417$) and $g = 0.328$. Type IV SI means type IV shock interference.

interval $t_{disturb}$, a disturbance of the density $\triangle\rho/\rho_0$. Since this is a contact discontinuity, the pressure and velocity are kept unchanged. This disturbance then causes a disturbance of the Mach number $M' = M_0\sqrt{1+\triangle\rho/\rho}$ so the disturbance $\triangle\rho < 0$ induces a decrease of Mach number to be above the detachment condition so that transition from RR to MR is made possible. The disturbance is either given in the entire height of the inlet, or is localised by giving the disturbance only in a height of $(1/20)H_A$ counting from the reflecting surface (approximately 10 cells). The duration $t_{disturb}$ of disturbance, measured with $\tau_{disturb} = t_{disturb}/(H_A/a_0)$ where a_0 is the sound speed at the inlet, is also a factor to be considered.

The initial RR result is obtained in a similar way as in the numerical simulation of § 3.2, i.e. we use a second-order Roe scheme in the same way as Bai & Wu (2021), and the grid number is 400×800. During transition calculation, unsteady calculation with second-order accuracy is used, with a time step of $\Delta t < 10^{-4}(H_A/a_0)$, following Li *et al.* (2011).

Several test cases with various values of these factors are given in table 4. Numerical simulation shows three situations: failure to inaugurate any MR, transition from RR to MR to unstart flow (here called direct transition) and transition from RR to MR to RR (here called inverted transition).

For case 1, the disturbance is applied locally in a stripe close to the reflected surface, with relatively small discontinuity and short duration. We observe no transition, i.e. no MR structure is produced at any time. For other conditions, we have either direct transition or inverted transition.

4.3. *Direct dynamic transition type I: from RR to MR to unstart*

Compared with case 1, cases 2 and 3 increase the intensity of the density disturbances. We observe 'RR to MR to unstart' transition. For case 4 and case 5, the duration of density is increased compared with case 1, and we also observe 'RR to MR to unstart' transition. Figure 9 displays for case 4 the Mach number at several stages of the transition process.

Stage 1: initial RR. The RR result, not displayed, is treated as the initial condition before the upstream disturbance is introduced.

Stage 2: disturbance propagation. The upstream disturbance is generated at the inlet, and then propagates toward the reflecting point. Figure 9(*a*) is the result at some instance. This upstream disturbance has not yet touched the reflection point so the RR configuration near the reflecting point is not yet affected.

Stage 3: disturbance RR interaction stage. The disturbance reaches the reflecting point and strengthens the incident shock at the reflecting point (figure 9*b*). Locally, the shock

https://doi.org/10.1017/jfm.2026.11335 Published online by Cambridge University Press

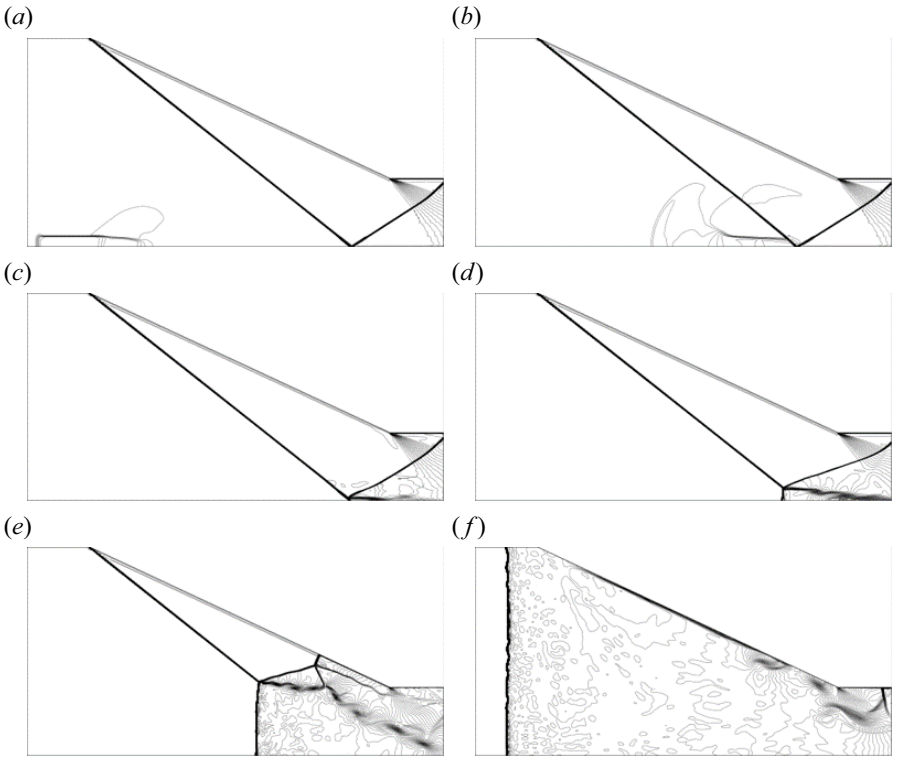


Figure 9. Mach number contours for direct dynamic transition type I (case 4 in table 4).

angle of the incident shock overtakes the detachment condition so the local RR structure transits to MR (figure 9*c*).

Stage 4: pseudo-steady MR stage (figure 9*d*). The density disturbance has fully transmitted the Mach stem and there remains a pure pseudo-steady MR structure. For conventional dynamic transition as considered by Kudyavtev *et al.* (2002) and Mouton & Hornung (2007), the MR will become stable. Here, since g lies within the dual-solution stability gap, the MR cannot be stabilised, and it will propagate towards the upstream direction.

Stage 5: unsteady double MR stage. The reflected shock of the pseudo-steady MR, after grazing the trailing edge, reflects at the lower wedge surface, and creates another pseudo-steady MR structure for the present condition. The lower MR and upper MR both propagate toward the inlet (figure 9*e*).

Stage 6: unstart subsonic flow (figure 9*f*). The double MR structure has touched the inlet and a shock is formed at the inlet. This shock would become a bow shock once a steady state could be reached. The flow downstream becomes subsonic, and corresponds to what we call unstart flow.

4.4. *Direct dynamic transition type II: from RR to MR + type IV shock interference to unstart*

For case 6, both the intensity of density disturbance and the duration of disturbance are increased compared with case 1. We observe the so-called direct transition type II, as displayed in figure 10, which shows the Mach number at several stages of the transition process.

https://doi.org/10.1017/jfm.2026.11335 Published online by Cambridge University Press

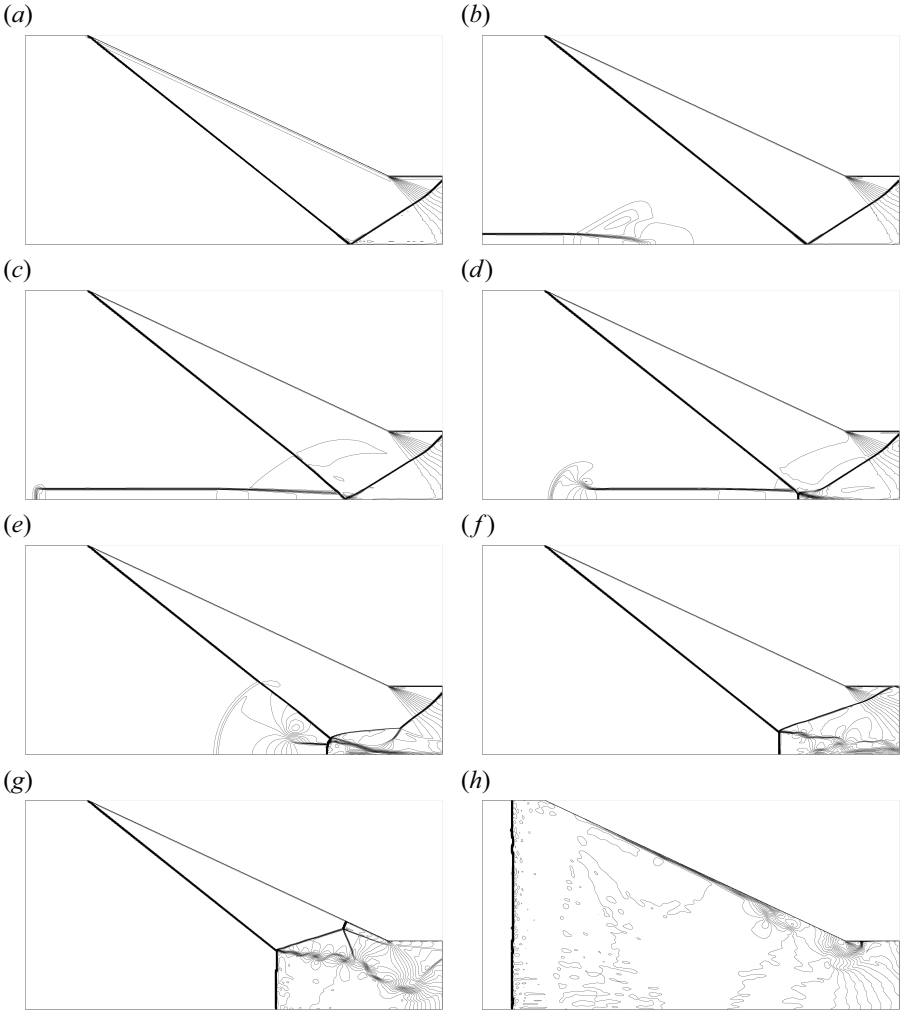


Figure 10. Mach number contours for direct dynamic transition (case 6 in table 4).

Stage 1: initial RR. The RR result, shown in figure 10(*a*), is treated as the initial condition before the upstream disturbance is introduced.

Stage 2: disturbance propagation. The upstream disturbance is generated at the inlet, and then propagates toward the reflecting point. Figure 10(*b*) is the result at $t \approx (1/2)t_{disturb}$. This upstream disturbance has not yet touched the reflection point so the RR configuration near the reflecting point is not yet affected.

Stage 3: disturbance RR interaction stage. The disturbance reaches the reflecting point and strengthens the incident shock at the reflecting point (figure 10*c*). For the present condition, this occurs at $t \approx t_{disturb}$, when the upstream disturbance at the inlet is terminated. Locally, the shock angle of the incident shock overtakes the detachment condition so the local RR structure transits to MR (figure 10*d*).

Stage 4: disturbed MR + type VI interference stage (figure 10*e*, see figure 11 for a schematic display). Note that type VI interference does not appear in direct dynamic transition type I. The Mach stem of MR is still subjected to the interaction of the upstream density disturbance. This disturbance has a slipline (*PM*) almost parallel to the reflecting

https://doi.org/10.1017/jfm.2026.11335 Published online by Cambridge University Press

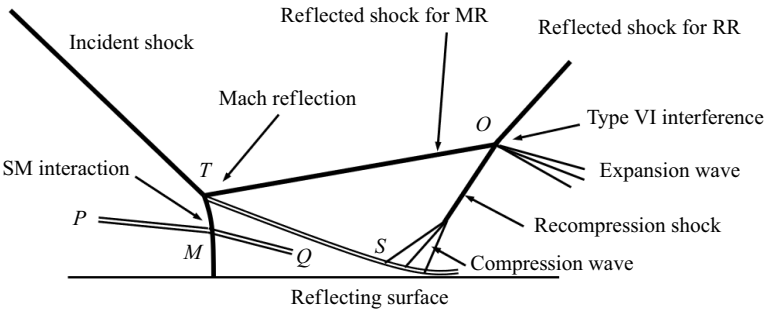


Figure 11. Schematic display of the MR + type VI interference. The *SM* interaction means the interaction between the edge of the density disturbance (slipline *PM*) and the Mach stem, which gives a transmitted slipline (*MQ*).

surface. The interaction between this slipline and the Mach stem, at point *M*, leads to a transmitted slipline (*MQ*). The type VI interference structure is composed of the reflected shock of MR, and a recompression shock over the turning point *S* of the slipline of MR. This interference leads to a shock that is one part of the reflected shock of the original RR. The recompression shock is due to the flow, which is initially parallel to the slipline, will be deflected to be parallel to the reflecting surface. Note that type VI interference also appears in the conventional dynamic transition problem studied by Kudyavtev *et al.* (2002) and Li *et al.* (2011).

Stage 5: pseudo-steady MR. The density disturbance has fully transmitted the Mach stem. Both this disturbance and the type VI interference structure have propagated far downstream, so there remains a pure pseudo-steady MR structure (figure 10*e*). For conventional dynamic transition as considered by Kudyavtev *et al.* (2002) and Mouton & Hornung (2007), the MR will become stable. Here, since *g* lies within the dual-solution stability gap, the MR cannot be stabilised, and it will propagate towards the upstream direction.

Stage 6: unsteady double MR stage. The reflected shock of the pseudo-steady MR, after grazing the trailing edge, reflects at the lower wedge surface, and creates another pseudo-steady MR structure for the present condition. The lower MR and upper MR both propagate toward the inlet (figure 10*f*).

Stage 7: unstart subsonic flow (figure 10*g*). The double MR structure has touched the inlet and a shock is formed at the inlet. The flow downstream becomes subsonic, and corresponds to what we call unstart flow.

4.5. *Inverted transition: from RR to MR to RR*

Figure 12 shows the results for case 7. The disturbance is applied to the whole inlet so the entire incident shock will be disturbed. We observed what we call here inverted transition.

Stage 1: RR to MR transition. This incident shock will be strengthened so it causes RR to MR transition once the disturbance has reached the reflecting point. Figure 12(*a*) displays the result at a moment when RR has transited to MR. The early stage during RR to MR transition is similar to the cases considered above and is not shown here.

Stage 2: weakening MR. The highly disturbed part of the incident shock is weakened by the ending part of the density disturbance, so the Mach stem reduces its height (figure 12*b*,*c*).

Stage 3: MR back into RR. The transition process is inverted, and the MR transits back into a highly disturbed RR (figure 12*d–f*).

https://doi.org/10.1017/jfm.2026.11335 Published online by Cambridge University Press

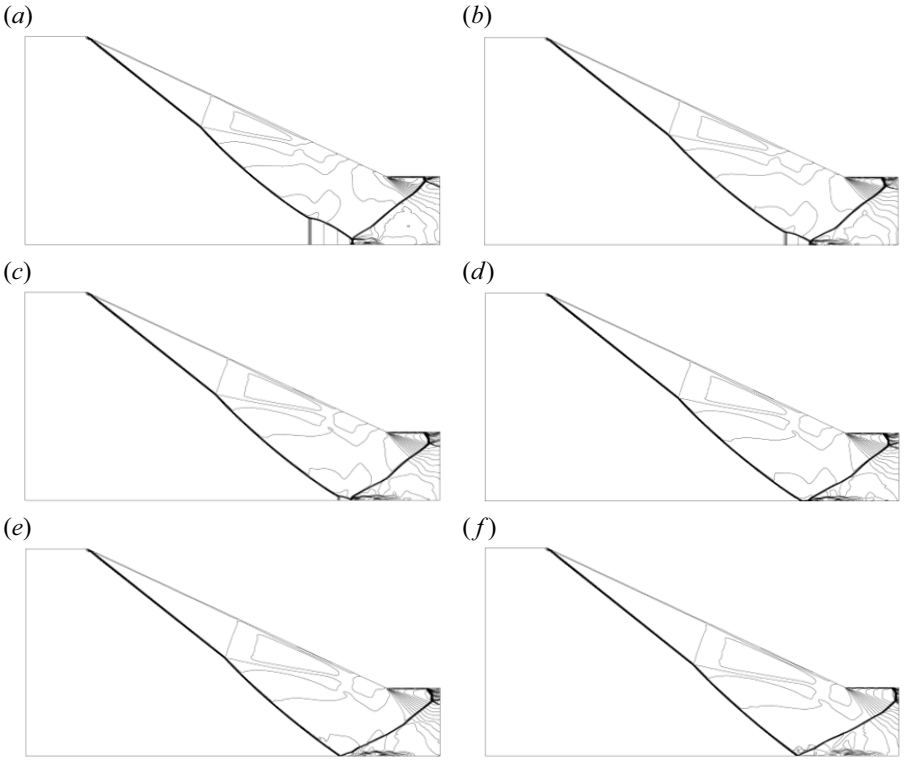


Figure 12. Mach number contours for inverted dynamic transition (case 7 in table 4).

Stage 4: stable RR. Finally, we get back the initial RR structure.

The inverted dynamic transition occurs when the density disturbance first strengthens the incident shock (so that detachment condition is reached) and then weakens the incident shock (so that von Neumann condition is reached).

5. Conclusions

In this paper, we have revisited the lower limit $H_{R,min}$ of the trailing-edge height, at which the reflective shock grazes the trailing edge and below which shock reflection may become unstable.

A major work is that we have proved that $H_{R,min}^{(MR)} > H_{R,min}^{(RR)}$, assumed by Li & Ben-Dor (1997) without proof, holds in a large part of the dual-solution domain. This would have not been possible since $H_{R,min}^{(MR)}$ depends on the Mach stem height. To overcome this difficulty, we have used proof by transitivity, through finding a lower bound of $H_{R,min}^{(MR)}$ that corresponds to the minimum Mach stem height. We have shown that $H_{R,min}^{(MR)} > H_{R,min}^{(RR)}$ holds within the dual-solution domain, sufficiently far away from the tip horn corner of the dual-solution domain. The proof of the inequality means that there indeed exists a dual-solution stability gap for H_R between the lower limit $H_{R,min}^{(RR)}$ (called the subcritical threshold) and the lower limit $H_{R,min}^{(MR)}$ (called the supercritical threshold). Above the supercritical threshold, both RR and MR can be stable, i.e. we may have steady stable RR and MR solutions in the dual-solution domain. Below the subcritical threshold, both

https://doi.org/10.1017/jfm.2026.11335 Published online by Cambridge University Press

RR and MR are unstable. Between the subcritical threshold and the supercritical threshold; RR is stable and MR is unstable.

A road map is given to obtain the accurate value of the quantity of the dual-solution stability gap. This roadmap combines the theory and numerical simulation. For three cases, we have shown that the dual-solution stability gap is large compared with the subcritical geometric threshold $H_{R,min}^{(RR)}$. The accuracy of the roadmap is further confirmed by numerical simulation.

The confirmation of the dual-solution stability gap implies a new transition possibility: within the dual-solution stability gap, i.e. for $H_{R,min}^{(RR)} < H_R < H_{R,min}^{(MR)}$, a stable RR can transit dynamically to unstable MR under suitable local disturbance. Previous studies about dynamic transition (cf. Kudyavtev *et al.* 2002; Mouton & Hornung 2007; Li *et al.* 2011) assumed implicitly $H_R > H_{R,min}^{(MR)}$, so dynamic transition leads to stable MR. Here, we indeed observe dynamic transition from stable RR to unstable MR, through numerical simulation with density perturbation, for the particular condition with $M_0 = 4$, $\theta_w = 25^o$ and $H_R = 0.328 H_A$.

Numerical simulation shows various types of dynamic transition and displays various complex shock interaction structures during dynamic transition within the dual-solution stability gap. One type is direct dynamic transition for which the transition goes from RR to MR to unstart flow. The other type is inverted dynamic transition, for which RR transits to MR but then transits back to RR. Complex flow structures, such as hybrid MR –type VI shock interference, and double MR–MR, are found to exist during the dynamic transition, depending on how we provide the disturbance.

Although Vuillon *et al.* (1995) suggested using the Mach stem height model of Azevedo & Liu (1993) to estimate the Mach stem height involved in the expression for the lower limit, the present study has avoided the use of approximate models since we need accurate values for the dual-solution stability gap. As shown by an example in Appendix A, using an approximate model to evaluate A and B and then using them in expressions (3.9) and (3.10) (§ 3) for the dual-solution stability gap may lead to significant errors.

The present study has focused on inviscid two-dimensional flow. In real flow, the wedge low surface has a boundary layer, which alters the effective wedge angle and the effective trailing-edge height (see Appendix B for a short discussion about how to make a simple correction accounting for the boundary-layer effect). Three-dimensional effects may also alter the stability gap. Threadgill & Little (2020) have shown that the swept angle of the leading edge affects shock reflections, by reducing the effective Mach number and altering the effective wedge angle. Thus, the swept angle effect may be accounted for through replacing the Mach number and wedge angle by their effective ones.

Acknowledgements. The authors thank the referees for their valuable comments leading to improvement of this manuscript.

Funding. This work was supported partly by the National Key Project (Grant no. GJXM92579) and by the National Science and Technology Major Project 2017-II-003-0015.

Declaration of interests. The authors report no conflict of interest.

Appendix A. Limitation of approximate modelling

This appendix is to report the stability gap when the coefficients A and B required in expression (3.9) (§ 3) are given by an approximate Mach stem height. The purpose here is to how the results based on simplified modelling may be not accurate compared with the

https://doi.org/10.1017/jfm.2026.11335 Published online by Cambridge University Press

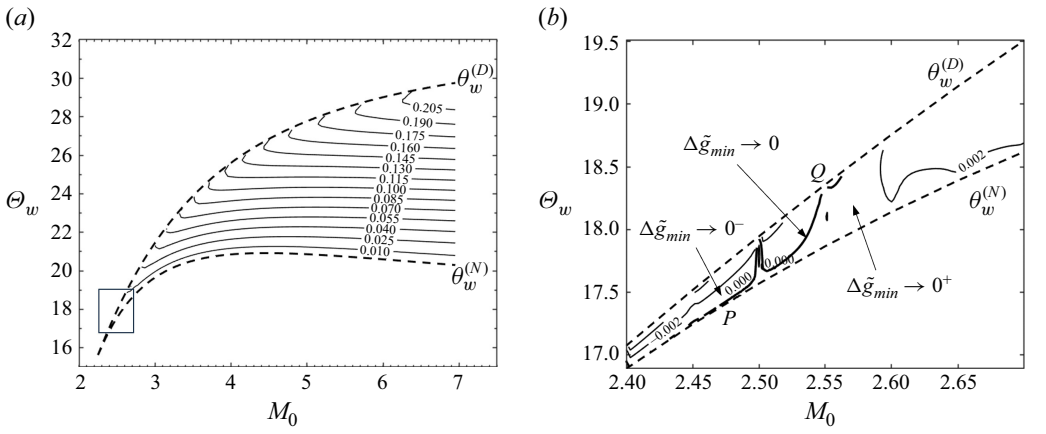


Figure 13. Contourlines of $\Delta\widetilde{g}_{min}$ give the approximate method; (*a*) global view, (*b*) enlarged view.

results obtained from the roadmap proposed in § 3. Since the work of Azevedo (1989) (see also Azevedo & Liu 1993), several Mach stem height models have been proposed (e.g. Li & BenDor 1997; Mouton & Hornung 2007; Gao & Wu 2010; Bai & Wu 2017; Bai & Wu 2021).

Now we try the approximate model of Bai & Wu (2021, equation (25)) for A and B to compute $\widetilde{g}_{min}^{(MR)} = \overline{g}_{min}^{(MR)}$ by (3.9).

The resulting value of $\Delta\widetilde{g}_{min} = \widetilde{g}_{min}^{(MR)} - g_{min}^{(RR)}$ by (3.10) is displayed in figure 13. For comparison we consider the three cases shown in table 2.

For case 1, we have $\Delta\overline{g}_{min} = 0.178$ according to table 2, while by figure 13, $\Delta\widetilde{g}_{min} \approx 0.12$. Thus, the difference between $\Delta\overline{g}_{min}$ and $\Delta\widetilde{g}_{min}$ is as large as 33 %. This means that, for case 1, the approximate method underestimates the dual-solution stability gap by 33 %.

Now consider case 2. We have $\Delta\overline{g}_{min} = 0.091$ according to table 2, while by figure 13, $\Delta\widetilde{g}_{min} \approx 0.03$. Thus, the approximate method underestimates the dual-solution stability gap by 67 %.

Last, we consider case 3. We have $\Delta\overline{g}_{min} = 0.185$ according to table 2, while by figure 13, $\Delta\widetilde{g}_{min} \approx 0.12$. Thus, the approximate method underestimates the dual-solution stability gap by 35 %.

In conclusion, the simplified modelling used above does not yield quantitative correct estimation of the dual-solution stability gap, and this is why we proposed the roadmap presented in § 3.

Appendix B. Discussion of the effect of the boundary layer

The present study is a two-dimensional inviscid study. Practical flow has a boundary layer. For shock reflection, there are two alternative ways to account for the effect of the boundary layer.

One is to use the shock angle β_{01} of the incident shock, as by Hornung & Robinson (1982) for experimental study and by Li & Ben-Dor (1997) for analytical study of the Mach stem height. Practically, the shock angle depends not only on M_0 and θ_w, but also on the thickness of the boundary layer, which in turn depends on the Mach number and Reynolds number. Using β_{01} automatically accounts for the effect of the boundary layer. To apply the present result which uses θ_w as one input parameter, we may, for each real β_{01} (which accounts for the boundary layer in a real situation), we use the shock angle

https://doi.org/10.1017/jfm.2026.11335 Published online by Cambridge University Press

relation

$$\tan\theta_w^{(e)} = f_\theta(M_0, \beta_{01}) \tag{B1}$$

to find the equivalent wedge angle $\theta_w^{(e)}$ (which accounts for the effect of the boundary layer). Then, we replace θ_w by $\theta_w^{(e)}$ in the theory presented in §§ 2 and 3, to obtain the dual-solution stability gap.

The second one is to use boundary-layer correction, by adding the displacement thickness correction to θ_w. Details of this method have been given by Chen *et al.* (2020), who provided an explicit method to evaluate the displacement thickness and its correction to θ_w, and showed that such a correction can effectively account for the effect of the boundary layer when compared with numerical simulation.

Chen *et al.* (2020) also showed that the boundary layer gives a correction to the effective trailing-edge height ($g^{(e)}$), and showed that the existence of the boundary layer reduces the trailing-edge height.

Overall, the boundary layer increases the effective θ_w or the shock angle, and reduces the effective trailing-edge height g. The introduction of the explicit formulas for the correction of θ_w and of g into the formulas of §§ 2 and 3 where θ_w and g are involved can yields the results when the boundary layer is considered. Thus, it is possible that the boundary-layer effects may not change the primary conclusions of this study, i.e. if the above correction is introduced so that the parameter space is replaced by the equivalent ones ($\theta_w^{(e)}$ and $g^{(e)}$), the predicted critical thresholds might remain applicable, and the observed stability or instability of the MR and RR structures might remain unchanged. However, a detailed consideration of this correction merits a study in the future.

References

Anderson, J.D. 2001 *Fundamentals of Aerodynamics*, 3rd edn. McGraw-Hill Higher Education.

Azevedo, D.J. 1989 Analytical prediction of shock patterns in a high-speed wedge bounded duct. PhD thesis, Department of Mechanical and Aerospace Engineering, State University of NY Buffalo.

Azevedo, D.J. & Liu, C.S. 1993 Engineering approach to the prediction of shock patterns in bounded high-speed flows. *AIAA J.* **31**, 83–90.

Baby, V.Y., Paramanantham, V. & Rajesh, G. 2024 RR–MR transition in short wedges. *J. Fluid Mech.* **998**, ArticleA38.

Bai, C.Y. 2023 Shock reflection with incident shock–wedge trailing-edge expansion fan interaction. *J. Fluid Mech.* **968**, A21.

Bai, C.Y. & Wu, Z.N. 2017 Size and shape of shock waves and slipline for Mach reflection in steady flow. *J. Fluid Mech.* **818**, 116–140.

Bai, C.Y. & Wu, Z.N. 2021 A study of the dependence of the Mach stem height on the trailing edge height. *Fluids* **6**, 313.

Ben-Dor, G., Elperin, T., Li, H. & Vasiliev, E. 1999 The influence of the downstream pressure on the shock wave reflection phenomenon in steady flows. *J. Fluid Mech.* **386**, 213–232.

Ben-Dor, G. 2007 *Shock Wave Reflection Phenomena*, 2nd edn. Springer.

Ben-Dor, G., Ivanov, M., Vasilev, E.I. & Elperin, T. 2002 Hysteresis processes in the regular reflection–Mach reflection transition in steady flows. *Prog. Aerosp. Sci.* **38**, 347–387.

Chen, Z.J., Bai, C.Y. & Wu, Z.N. 2020 Mach reflection in steady supersonic flow considering wedge boundary-layer correction. *Chinese J. Aeronaut.* **33** (2), 465–475.

Chpoun, A., Passerel, D., Li, H. & Ben-Dor, G. 1995 Reconsideration of oblique shock wave reflections in steady flows. Part 1. Experimental investigation. *J. Fluid Mech.* **301**, 19–35.

Felthun, L.T. & Skews, B.W. 2002 Transition between regular and Mach reflection in dynamic compressible flows. *AIAA Paper* AIAA-2002-0549.

Felthun, L.T. & Skews, B.W. 2004 Dynamic shock wave reflection. *AIAA J.* **42** (8), 1633–1639.

Gao, B. & Wu, Z.N. 2010 A study of the flow structure for Mach reflection in steady supersonic flow. *J. Fluid Mech.* **656**, 29–50.

Goyal, R., Sameen, A., Jayachandran, T. & Rajesh, G. 2021 Dynamic effects in transition from regular to Mach reflection in steady supersonic flows. *Phys. Rev. E* **104**, 055101.

https://doi.org/10.1017/jfm.2026.11335 Published online by Cambridge University Press

GRASSO, F. & PAOLI, R. 1999 An analytical study of Mach reflection in nonequilibrium steady flows. *Phys. Fluids* **11** (10), 3150–3167.
GUAN, X.K., BAI, C.Y. & WU, Z.N. 2018 Steady Mach reflection with two incident shock waves. *J. Fluid Mech.* **855**, 882–909.
HE, Y. & SHI, A. 2025 Transition of shock reflection with downstream expansion fan interference. *J. Fluid Mech.* **1007**, ArticleA5.
HEKIRI, H. & EMANUEL, G. 2015 Structure and morphology of a triple point. *Phys. Fluids* **27**, 056102.
HENDERSON, L.F. & LOZZI, A. 1975 Experiments on transition of Mach reflection. *J. Fluid Mech.* **68**, 139–155.
HENDERSON, L.F. & LOZZI, A. 1979 Further experiments on transition to Mach reflection. *J. Fluid Mech.* **94**, 541–559.
HORNUNG, H.G. 1986 Regular and Mach reflections of shock waves. *Annu. Rev. Fluid Mech.* **18**, 33–58.
HORNUNG, H.G. 2014 Mach reflection in steady flow. I. Mikhail Ivanov's contributions, II. Caltech stability experiments. *AIP Conf. Proc.* **1628**, 1384–1393.
HORNUNG, H.G., OERTEL, H. & SANDEMAN, R.J. 1979 Transition to Mach reflection of shock waves in steady and pseudo-steady flows with and without relaxation. *J. Fluid Mech.* **90**, 541–560.
HORNUNG, H.G. & ROBINSON, M.L. 1982 Transition from regular to Mach reflection of shock waves. Part 2. The steady-flow criterion. *J. Fluid Mech.* **123**, 155–164.
IVANOV, M.S., KLEMENKOV, G.P., KUDRYAVTSEV, A.N., FOMIN, V.M. & KHARITONOV, A.M. 1997 Experimental investigation of transition to Mach reflection of steady shock waves. *Dokl. Akad. Nauk* **357** (5), 623–627.
IVANOV, M.S., KUDRYAVTSEV, A.N. & KHOTYANOVSKII, D.V. 2000 Numerical simulation of the transition between the regular and Mach reflection of shock waves under the action of local perturbations. *Dokl. Phys.* **45** (7), 353–357.
IVANOV, M.S., MARKELOV, G.N., KUDRYAVTSEV, A.N. & GIMELSHEIN, S.F. 1998 Numerical analysis of shock wave reflection transition in steady flows. *AIAA J.* **36** (11), 2079–2086.
IVANOV, M.S., GIMELSHEIN, S.F. & MARKELOV, G.N. 1998 Statistical simulation of the transition between regular and Mach reflection in steady flows. *Comput. Maths Applics* **1** (2), 113–125.
IVANOV, M.S., BEN-DOR, G., ELPERIN, T., KUDRYAVTSEV, A.N. & KHOTYANOVSKY, D.V. 2001 Flow-Mach-number-variation-induced hysteresis in steady shock wave reflections. *AIAA J.* **39** (5), 972–974.
KUDRYAVTSEV, A.N., KHOTYANOVSKY, D.V., IVANOV, M.S. & VANDROMME, D. 2002 Numerical investigations of transition between regular and Mach reflections caused by free-stream disturbances. *Shock Waves* **12**, 157–165.
LI, H. & BEN-DOR, G. 1996 Application of the principle of minimum entropy production to shock wave reflections. I. Steady flows. *J. Appl. Phys.* **80**, 2027–2037.
LI, H. & BEN-DOR, G. 1997 A parametric study of Mach reflection in steady flows. *J. Fluid Mech.* **341**, 101–125.
LI, H., CHPOUN, A. & BEN-DOR, G. 1999 Analytical and experimental investigations of the reflection of asymmetric shock waves in steady flows. *J. Fluid Mech.* **390**, 25–43.
LI, S.G., GAO, B. & WU, Z.N. 2011 Time history of regular to Mach reflection transition in steady supersonic flow. *J. Fluid Mech.* **682**, 160–184.
MARGHA, L., HAMADA, A.A. & ELTAWEEL, A. 2023 Dynamic transition of unsteady supersonic flow from Mach to regular reflection over a moving wedge. *ASME J. Fluids Engng* **145** (9), 091201.
MOUTON, C.A. & HORNUNG, H.G. 2007 Mach stem height and growth rate predictions. *AIAA J.* **45** (8), 1977–1987.
NAIDOO, K. & SKEWS, B.W. 2011 Dynamic effects on the transition between two-dimensional regular and Mach reflection of shock waves in an ideal, steady supersonic free stream. *J. Fluid Mech.* **676**, 432–460.
NAIDOO, K. & SKEWS, B.W. 2014 Dynamic transition from Mach to regular reflection of shock waves in a steady flow. *J. Fluid Mech.* **750**, 385–400.
ROYE, L., HENDERSON, F. & MENIKOFF, R. 1998 Triple-shock entropy theorem and its consequences. *J. Fluid Mech.* **366**, 179–210.
SCHOTZ, M., LEVY, A., BEN-DOR, G. & IGRA, O. 1997 Analytical prediction of the wave configuration size in steady flow Mach reflections. *Shock Waves* **7**, 363–372.
TAN, L.H., REN, Y.X. & WU, Z.N. 2006 Analytical and numerical study of the near flow field and shape of the Mach stem in steady flows. *J. Fluid Mech.* **546**, 341–362.
THREADGILL, J.A.S. & LITTLE, J.C. 2020 An inviscid analysis of swept oblique shock reflections. *J. Fluid Mech.* **890**, A22.

https://doi.org/10.1017/jfm.2026.11335 Published online by Cambridge University Press

TESHUKOV, V.M. 1989 On stability of RR of shock waves. *Prikl. Mekh. Tekh. Fiz.* **2**, 26–33.
VON NEUMANN, J. 1943 Oblique reflection of shock. Explosives Research Report 12. Navy Department, Bureau of Ordnance, Washington, DC.
VUILLON, J., ZEITOUN, D. & BEN-DOR, G. 1995 Reconsideration of oblique shock wave reflections in steady flows. Part 2. Numerical investigation. *J. Fluid Mech.* **301**, 37–50.

https://doi.org/10.1017/jfm.2026.11335 Published online by Cambridge University Press